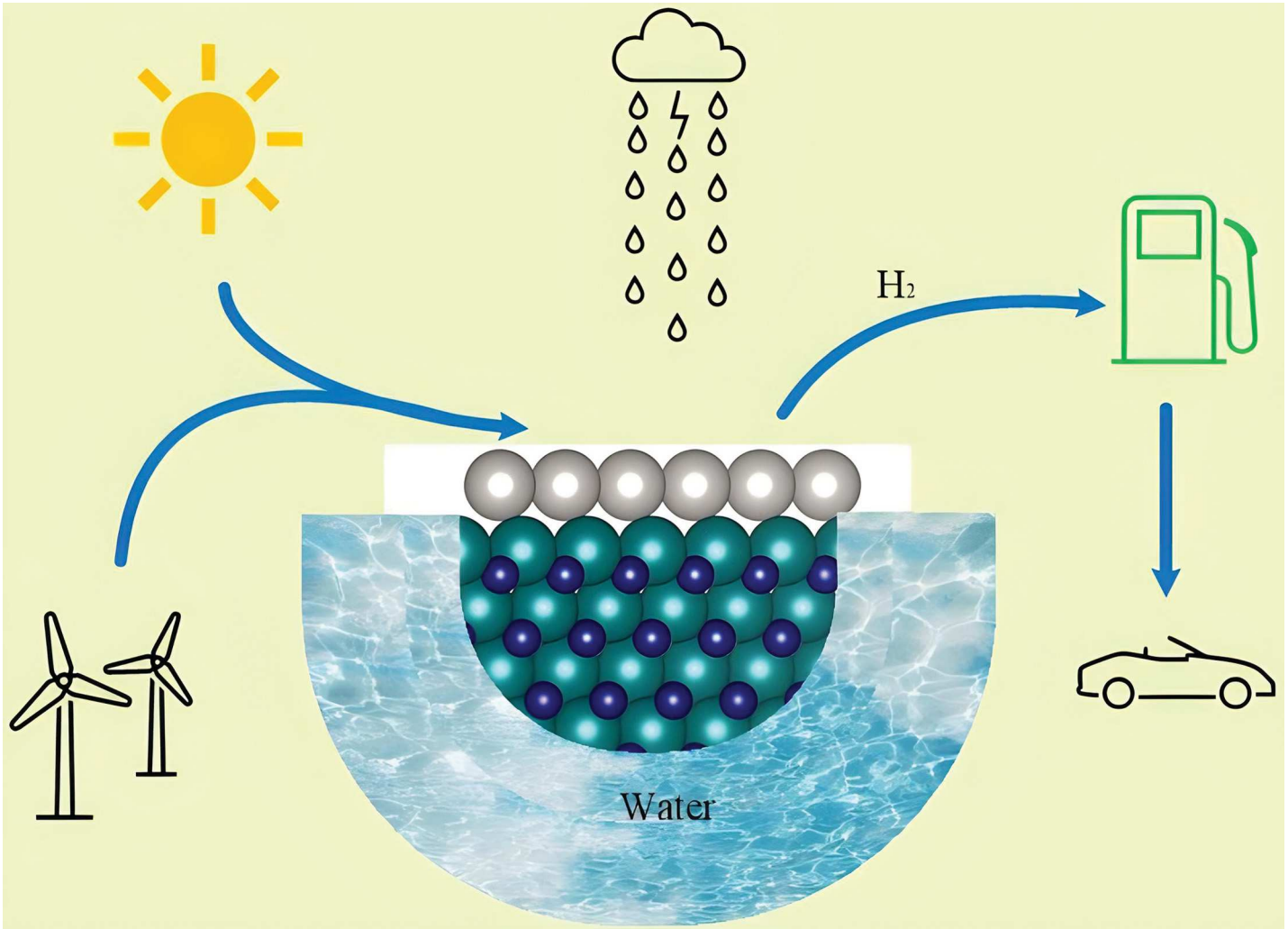

Showcasing research from Prof. Shyam Kattel's computational catalysis laboratory at the Department of Physics, Florida A&M University, Florida, USA

Pt- and Pd-modified transition metal nitride catalysts for the hydrogen evolution reaction

We study Pt and Pd modified TMNs as low-cost HER catalysts. Our calculations show that Pt and Pd bind strongly with TM on TMN(111) surfaces, leading to the formation of stable Pt/Pd-monolayer(ML)–TMN(111) structures. Furthermore, our calculated hydrogen binding energy demonstrates that several Pt, Pd/TMN are promising candidates for HER with a low value of limiting potential similar to that calculated on Pt(111).

As featured in:

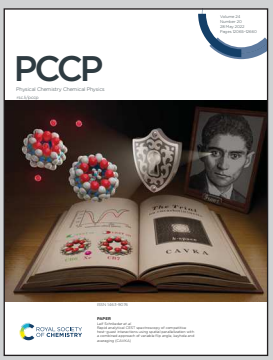

See Damilola Ologunagba and Shyam Kattel, *Phys. Chem. Chem. Phys.*, 2022, **24**, 12149.

ROYAL SOCIETY OF CHEMISTRY

rsc.li/pccp

Registered charity number: 207890

PCCP

ROYAL SOCIETY OF CHEMISTRY

PAPER

Cite this: *Phys. Chem. Chem. Phys.*, 2022, **24**, 12149

Pt- and Pd-modified transition metal nitride catalysts for the hydrogen evolution reaction

Damilola Ologunagba and Shyam Kattel *

Received 16th February 2022,
Accepted 6th April 2022

DOI: 10.1039/d2cp00792d

rsc.li/pccp

Hydrogen production *via* electrochemical splitting of water using renewable electricity represents a promising strategy. Currently, platinum group metals (PGMs) are the best performing hydrogen evolution reaction (HER) catalysts. Thus, the design of non-PGM catalysts or low-loading PGM catalysts is essential for the commercial development of hydrogen generation technologies *via* electrochemical splitting of water. Here, we employed density functional theory (DFT) calculations to explore Pt and Pd modified transition metal nitrides (TMNs) as low-cost HER catalysts. Our calculations show that Pt/Pd binds strongly with TMs on TMN(111) surfaces, leading to the formation of stable Pt and Pd–monolayer (ML)–TMN(111) structures. Furthermore, our calculated hydrogen binding energy (HBE) demonstrates that Pt/MnN, Pt/TiN, Pt/FeN, Pt/VN, Pt/HfN, Pd/FeN, Pd/TaN, Pd/NbN, Pd/TiN, Pd/HfN, Pd/MnN, Pd/ScN, Pd/VN, and Pd/ZrN are promising candidates for the HER with a low value of limiting potential (U_L) similar to that calculated on Pt(111).

1. Introduction

Hydrogen is an attractive alternative clean fuel.[1–3] However, currently, hydrogen is produced primarily *via* catalytic reforming of hydrocarbons and alcohols using precious metal catalysts.[4,5] This fossil fuel-based production of hydrogen is not sustainable and also energy-intensive as reforming is typically carried out at high temperatures.[6,7] In this regard, ambient condition electrochemical water splitting to produce hydrogen is appealing.[8–12] Electrochemical hydrogen production, when carried out using renewable electricity, represents a carbon neutral sustainable approach for producing hydrogen that can be used as a clean fuel.[13–16]

Electrochemical splitting of water consists of two half-reactions: a hydrogen evolution reaction (HER) that occurs at the cathode and an oxygen evolution reaction (OER) that occurs at the anode. The HER at the cathode can proceed *via* the Volmer–Heyrovsky or Volmer–Tafel mechanism.[17–21] In acidic solution, the elementary steps in the HER are[17]

$$H^+ + e^- \rightarrow H^* \quad \text{Volmer reaction}$$

$$H^* + H^+ + e^- \rightarrow H_2\,(g) + * \quad \text{Heyrovsky reaction}$$

$$H^* + H^+ \rightarrow H_2\,(g) + * \quad \text{Tafel reaction}$$

Along the Volmer–Heyrovsky reaction pathway,[22] the HER proceeds *via* the Volmer step followed by the Heyrovsky step. The Volmer step involves an electron transfer to a proton to produce an adsorbed hydrogen (H*) on the catalyst surface. In the Heyrovsky step, the electron-coupled proton transfer to H* produces H_2(g). Along the Volmer–Tafel mechanism,[22] the HER proceeds *via* the Volmer reaction described above to form surface-bound H*, and the Tafel step involves the combination of two H* to produce H_2(g).

Platinum group metals (PGMs): Pt and Pd are the most stable and active catalysts for the HER.[23–26] The high cost associated with PGM catalysts severely limits their large-scale application as HER catalysts.[27–29] Thus, reducing the loading of the PGM in the catalyst design without compromising the activity is a promising strategy to develop low-cost and effective HER catalysts.[30–33] The core@shell architecture[34] consisting of low-cost core materials with a thin PGM shell has been demonstrated to exhibit similar or even higher HER activity compared to PGM catalysts.[35] Several types of such catalyst structures having less expensive core metals with Pt and Pd thin shells (ranging from a monolayer to a few atomic layers) have been studied for many electrochemical reactions, including the HER using experimental and theoretical methods.[22,36,37]

Transition metal carbides (TMCs), transition metal phosphides (TMPs), transition metal borides (TMBs), and transition metal nitrides (TMNs) have been explored as electrocatalysts for the HER.[38–62] Abghoui *et al.*[54] reported that TaN, HfN, MoN, and ScN catalyze the HER at overpotentials between −0.09 V and −0.34 V. Peterson *et al.*[63] demonstrated that the activity of TMC catalysts is between low activities shown by early transition metals and high activities shown by compounds of Pt/Pt-group metals. In addition to the above, TMPs have also been explored as potential catalysts for the HER, including the phosphides of Co, Ni, and Fe.[11]

Department of Physics, Florida A&M University Tallahassee, FL 32307, USA. E-mail: shyam.kattel@famu.edu

In this study, density functional theory (DFT) calculations are performed to study the HER on Pt and Pd monolayers on less expensive TMNs. A monolayer of Pt and Pd is optimized on the (111) surface of TMNs, and the DFT calculated hydrogen binding energy is used to predict a set of promising HER candidates. The results show that the monolayers of Pt/MnN, Pt/FeN, Pd/TaN, Pd/NbN, Pd/TiN, Pd/HfN, Pd/MnN, Pd/ScN, Pd/VN, and Pd/ZrN are promising candidates for the HER.

2. Computational methods

Periodic density functional theory (DFT)[64] calculations are performed using the Vienna *Ab Initio* Simulation Package (VASP).[65,66] All the DFT calculations are performed at the GGA level within the PAW–PW91[67,68] formalism and are spin-polarized.

The bulk structures of transition metal nitrides (TMNs) are modeled using the rock salt NaCl structure with an equal ratio of the transition metal (TM) and nitrogen (N). The unit cell of bulk TMNs contains four TM atoms and four N atoms. The DFT optimized bulk TMNs are used to cleave the TM terminated TMN(111) surfaces. The TMN(111) surfaces are modeled using a 4 bilayer (each containing one layer of the TM and N) 3×3 surface slabs. A monolayer of Pt and Pd is placed on optimized TMN(111) surfaces to model the Pt/Pd monolayer TMN [Pt/Pd–ML–TMN(111)] surfaces.

A vacuum of approximately 18 Å is added to the surface in the *z*-direction to minimize the artificial interactions between the slab and their periodic images. All the calculations are carried out using a plane-wave basis set of 400 eV energy cutoff, and a $3 \times 3 \times 1$ Monkhrost-Pack grid is used to carry out the Brillion zone integration.[69] Based on our experience,[70–72] the energy cutoff (400 eV) and *k*-point sampling ($3 \times 3 \times 1$) are large enough to obtain converged reaction energetics. During calculations, the atoms in the bottom two layers are fixed while all other atoms are allowed to relax until the Hellman–Feynman force on each ion is less than 0.02 eV $Å^{-1}$.

The formation energy (E_f) of the bulk unit cell is calculated as

$$E_f = \text{energy(bulk unit cell)} - n^* \text{ energy (TM)} - n/2^*\text{energy}(N_2) \quad (1)$$

where energy(bulk unit cell) is the total energy of the TMN unit cell, energy(TM) is the total energy of the TM in the energetically most favorable bulk phase, energy(N_2) is the total energy of a N_2 molecule in the gas phase, and n is the number of TM and N atoms in the TMN unit cell.

The surface energy of relaxed TMN(111) (σ^r) is calculated following the approach described in the study by Quesne *et al.*[73]

$$\sigma^r = \frac{E_{relax} - nE_{bulk}}{A} - \sigma^u \quad (2)$$

where the surface energy of unrelaxed TMN(111) (σ'') is given by

$$\frac{E_{slab} - nE_{bulk}}{2A} \quad (3)$$

Here, E_{relax} is the energy of the relaxed slab, E_{bulk} is the energy of the bulk unit cell, A is the surface area of the slab, and n is the number of bulk unit cells required to form TMN(111) slabs.

The binding energy (BE) of the adsorbate on the surface is calculated as

$$\text{BE(adsorbate)} = E(\text{slab + adsorbate}) - E(\text{slab}) - E(\text{adsorbate}) \quad (4)$$

where E(slab + adsorbate), E(slab), and E(adsorbate) are the total energies of the slab with the adsorbate, clean slab, and adsorbate in the gas phase, respectively.

The free energy changes (ΔG) are calculated using the computational hydrogen electrode (CHE) model developed by Norskov and coworkers.[74] In this model, the chemical potential of a proton-electron pair ($H^+ + e^-$) is equal to half of the chemical potential of the hydrogen gas molecule ($1/2\ \mu(H_2)$) at zero applied potential (U). Thus, the total chemical potential of the ($H^+ + e^-$) pair as a function of the applied potential (U), at all temperature and pH values, can be calculated as $\mu(H^+ + e^-) = \frac{1}{2}\mu(H_2(g)) - eU$.

The CHE model is employed at $U = 0$ V to construct free energy diagrams (ΔG *vs.* reaction coordinates) of the HER. The Gibbs free energy (G) of a species is calculated as[74]

$$G = E + ZPE - TS \quad (5)$$

Here, E is the total energy of a species obtained from DFT calculations, ZPE and S are the zero-point energy and entropy of a species, respectively, and T = 298.15 K.

Similar to a previous approach,[75] canonical ensemble (*NVT*) *ab initio* molecular dynamics (AIMD) simulations on few selected Pt, Pd/TMNs candidates are performed at 1000 K for 5 ps using the VASP code.

3. Results and discussion

TMCs and TMNs typically exist in two common crystal phases: a face centered cubic rocksalt and a hexagonal close pack (HCP).[72,76–81] In particular, many of these TMNs (e. g. NbN, VN, ZrN, RuN, TiN, CrN, and CoN) in rocksalt structures have been synthesized in previous experimental studies.[82–87] Therefore, we focus on the HER activity of 3d–5d TMNs in the rocksalt phase. TMNs in other bulk phases will be our interest in future studies. Firstly, DFT calculations are performed to compute the lattice constant and formation energies (E_fs) of 3d–5d TMNs in the rocksalt (NaCl: space group = $Fm\bar{3}m$) bulk structure. The DFT calculated lattice constants in Fig. 1 show a correlation between the DFT calculated lattice constants and atomic radii of TMs in TMNs (except for ZnN), indicating that the lattice constant of the bulk TMN is primarily determined by the size of TMs. The correlation observed between the DFT calculated lattice constants of TMNs and atomic radii of TMs suggests that an advanced machine learning (ML) scheme can be developed to fit the lattice constant with the elemental properties of TMs as illustrated in our previous study.[88] Such a ML study, which requires a sizeable data set, will also help in

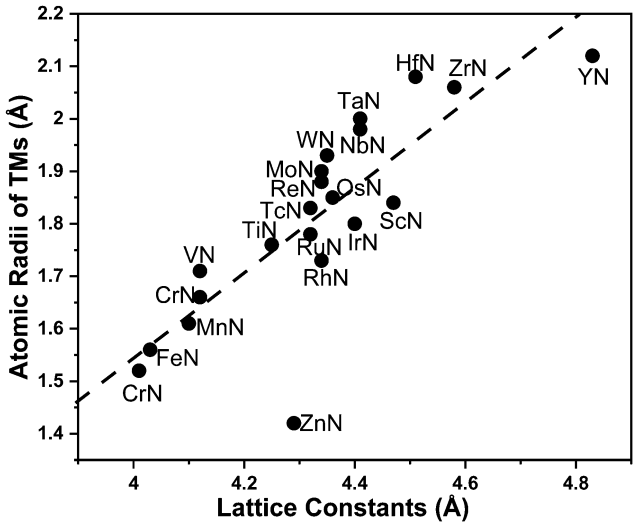

Fig. 1 Plot showing the relationship between the atomic radii of TMs (Å) and their lattice constants (Å).

identifying the most important feature related to the target property (lattice constant in this case). Our calculated E_fs in Table 1 show negative E_fs for CrN, HfN, MnN, MoN, NbN, ScN, TaN, TiN, VN, YN, and ZrN and small positive E_fs for AgN, AuN, CuN, FeN, IrN, NiN, ReN, RhN, RuN, TcN, WN, and ZnN. The positive E_f indicates the thermodynamically unfavorable formation of AgN, CoN, CuN, FeN, ZnN, AuN, IrN, NiN, ReN, RhN, RuN, TcN, and WN. Therefore, these TMNs are not included in the subsequent discussion of the HER activity. Secondly, we calculated the surface energies of TM-terminated-TMN(111) surfaces, which represent the thermodynamically most stable facet of the face centered cubic rocksalt phase. Furthermore, a strong interaction between the TM terminated surfaces of TMNs/TMCs and Pt/Pt is expected due to similar electronic structures of TMNs/TMCs and Pt/Pt leading to stable Pt/Pd overlayers.[82,89–91] The DFT calculated surface energies (Table 1) are all positive, except for TcN, and are similar to those reported for transition metal carbides (TMCs).[73] TMCs have been successfully synthesized and studied as catalysts for thermo/electro-catalytic reactions.[92] The negative E_f of several of TMNs and their comparable surface energies of the (111) facets to TMC counterparts suggest that TMNs represent a new set of materials worthy of further investigation for application in catalysis.

Next, DFT calculations are performed to optimize a monolayer (ML) of Pt and Pd (9 Pt/Pd atoms) on the optimized TMN(111) surfaces. The Pt/Pd overlayer on TMN(111) mimics the TMN@Pt core@shell structure. This kind of architecture has been shown to reduce not only the precious metal loadings but also improve the catalytic performance for electrocatalytic reactions.[93–97] Pt/Pd atoms are placed on two different hollow sites (Fig. 2) to obtain the most favorable Pt/Pd–ML–TMN(111) surfaces. The results indicate that Pt is more stable at the hcp hollow site on CrN, HfN, and VN. In contrast, Pt is more favorably adsorbed at the fcc hollow sites on CuN, FeN, MnN, and TiN. In addition, the results also show that the hcp hollow site is the energetically most favorable site for Pd on HfN, NbN, TaN, and ZrN. On the other hand, the fcc hollow site is the most favorable site for Pd on CrN, CuN, FeN, MnN, ScN, TiN, and ZnN. The most favorable Pt–ML–TMN(111) (*i.e.* Pt ML adsorbed at the hcp hollow site on CrN, HfN, TaN, NbN, and VN and at the fcc hollow site on CuN, FeN, TiN, and ZnN) and Pd–ML–TMN(111) (*i.e.* Pd ML adsorbed at the hcp hollow site on HfN, NbN, TaN, VN, and ZrN and the fcc hollow site on CuN, FeN, MnN, ScN, TiN, and ZnN) are used for the calculations of the H binding energy (HBE) as discussed below. It is observed that Pt/Pd forms a strong bond with the TM on TMN(111) as indicated by the negative binding energies listed in Fig. 3. This

Table 1 Lattice constants (in Å) and formation energies per atom (eV per atom) of the bulk TMNs, and surface energies (Jm^{-2}) of TMN(111) surfaces

TMNs	Lattice constant (Å)	E_f/atom (eV per atom)	Surface energies (Jm^{-2})
AgN	4.56	1.61	0.42
AuN	4.62	1.71	0.39
CoN	4.01	-	0.83
CrN	4.12	−0.39	-
CuN	4.17	0.99	0.79
FeN	4.03	0.19	0.88
HfN	4.51	−1.82	0.98
IrN	4.40	1.45	1.11
MnN	4.10	−0.28	0.94
MoN	4.34	−0.04	0.58
NbN	4.41	−1.04	0.63
NiN	4.07	0.58	0.76
ReN	4.34	1.00	0.39
RhN	4.34	0.91	0.59
RuN	4.32	0.88	0.57
ScN	4.47	−1.99	1.24
TaN	4.41	−0.91	0.62
TcN	4.32	0.51	−0.03
TiN	4.25	−1.74	1.26
VN	4.12	−1.02	0.91
WN	4.35	0.25	0.46
YN	4.83	−1.60	0.78
ZnN	4.29	0.66	0.79
ZrN	4.58	−1.74	0.96

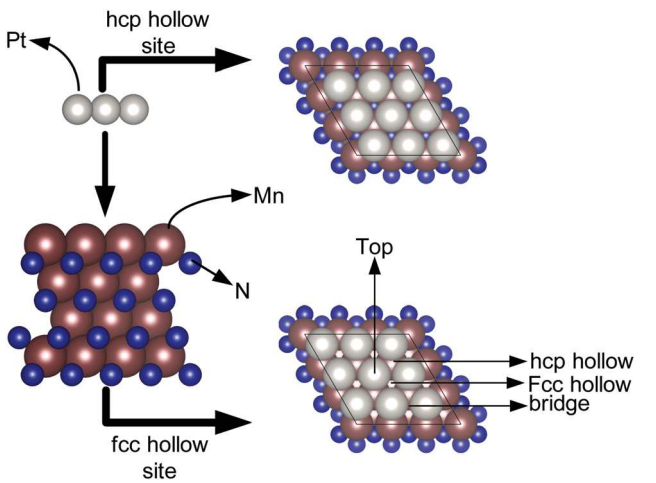

Fig. 2 Schematics of how Pt/Pd–ML–TMN(111) are formed in the present study. TM (in TMNs): brown, Pt: gray, and N: blue.

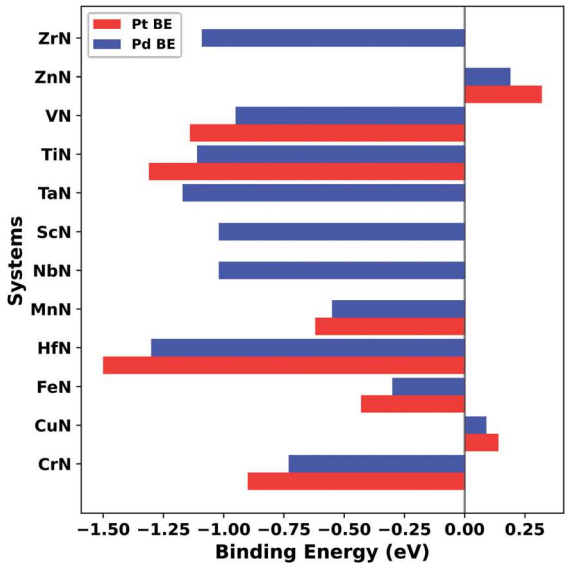

Fig. 3 DFT calculated BE (in eV) per atom of Pt and Pd on TMN (111) surfaces.

is due to the similar electronic structure of TMNs and Pt/Pd.[98–101] Thus, Pt/Pd ML–TMN(111) structures are expected to be stable for their potential application as HER catalysts.

The DFT optimized most stable structures of Pt/Pd–ML–TMN(111) are used to calculate the BEs of Pt and Pd on the TMN(111) surfaces. We found that Pt binds more strongly to CrN, FeN, HfNO, MnN, TiN, and VN compared to CuN and ZnN (Fig. 3). On the other hand, Pd binds more strongly to CrN, FeN, HfN, MnN, NbN, ScN, TaN, TiN, VN, and ZrN compared to CuN and ZnN (Fig. 3). Both Pt and Pd bind weakly to the CuN and ZnN surfaces compared to all the other surfaces. The positive Pt/Pd binding energy on Pt/Pd ML on CuN and ZnN suggests that there is a weak interaction between Pt/Pd and Cu/Zn. This makes Pt/Pd more reactive as evidenced by the strong HBE (Fig. 4). We notice that there is a significant movement of Pt/Pd atoms during optimization leading to the formation of the Pt/Pd cluster upon H adsorption, indicating the adsorbate induced cluster formation. This behavior shows that Pt/Pd ML on MoN and YN are unstable; therefore, Pt/Pd–ML–MoN(111) and Pt/Pd–ML–YN(111) are excluded from the subsequent discussions of the HER.

The Sabatier principle suggests that too strong HBE poisons the catalyst surface and leaves no free sites for further H binding, whereas too weak HBE requires higher overpotential for H adsorption.[102–104] Thus, an ideal catalyst should have an optimal HBE: neither too strong nor too weak. Previous experimental and theoretical studies have confirmed that the Gibbs free energy change of adsorbed hydrogen $\left(\Delta G_{\mathrm{H}}^{*}\right)$, which can be computed using the DFT calculated HBE[105] is the key descriptor of HER activity. Therefore, calculations of the HBE would allow us to evaluate the $\Delta G_{\mathrm{H}}^{*}$, which in turn can be used to predict the HER activity of the catalysts qualitatively. Using this approach, the DFT calculations are performed to calculate the HBE on the stable Pt/Pd–ML–TMN(111) surfaces (Fig. 4) to obtain the $\Delta G_{\mathrm{H}}^{*}$. All the four adsorption sites, 2-hollow (fcc and hcp), 1 top and 1 bridge as shown in Fig. 2, are considered for the calculations of the HBE. The optimized DFT structures show that the fcc hollow site is the most favorable site for the adsorption of hydrogen on Pt/CrN, Pd/TaN, and Pd/ZnN, while the most favorable site is the hcp hollow for Pt/FeN, Pt/HfN, Pt/MnN, Pt/TiN, Pt/VN, Pd/CuN, Pd/CrN, Pd/FeN, Pd/HfN, Pd/MnN, Pd/NbN, Pd/ScN, Pd/TiN, Pd/VN, and Pd/ZrN.

We found that the H binding on CrN, CuN, and ZnN is stronger than that on Pt(111), while the H adsorption is weaker on FeN, HfN, MnN, TiN, and VN compared to that on Pt(111). Similarly, the H binding on Pd/CuN and Pd/ZrN is stronger than that on Pt(111), while the H adsorption is weaker on Pd/FeN, Pd/HfN, Pd/MnN, Pd/NbN, Pd/TaN, Pd/TiN, Pd/VN, and Pd/ZrN compared to that on Pt(111). The H binding energy on Pd/ScN is similar to that on Pt(111).

The DFT calculated HBEs are then used to compute the $\Delta G_{\mathrm{H}}^{*}$ as described in eqn (5) and the results are plotted as shown in Fig. 5(a and b). Our computed $\Delta G_{\mathrm{H}}^{*}$ values in Fig. 5(a) show that Pt/MnN and Pt/TiN have the $\Delta G_{\mathrm{H}}^{*}$ value close to zero (0.003 eV and 0.02 eV, respectively) and are predicted to be the best

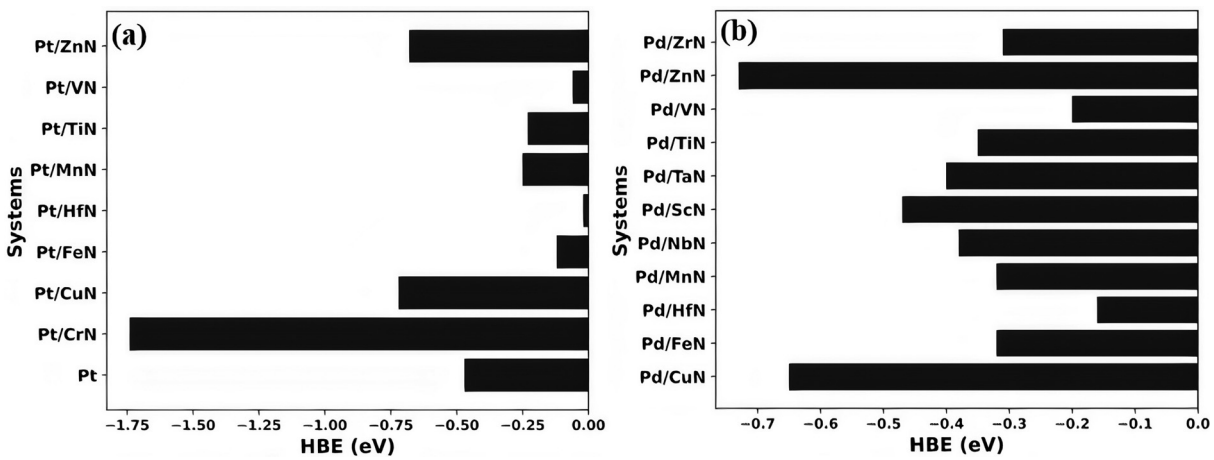

Fig. 4 DFT calculated HBEs (in eV) on (a) Pt/TMN(111) and (b) Pd/TMNs(111) surfaces.

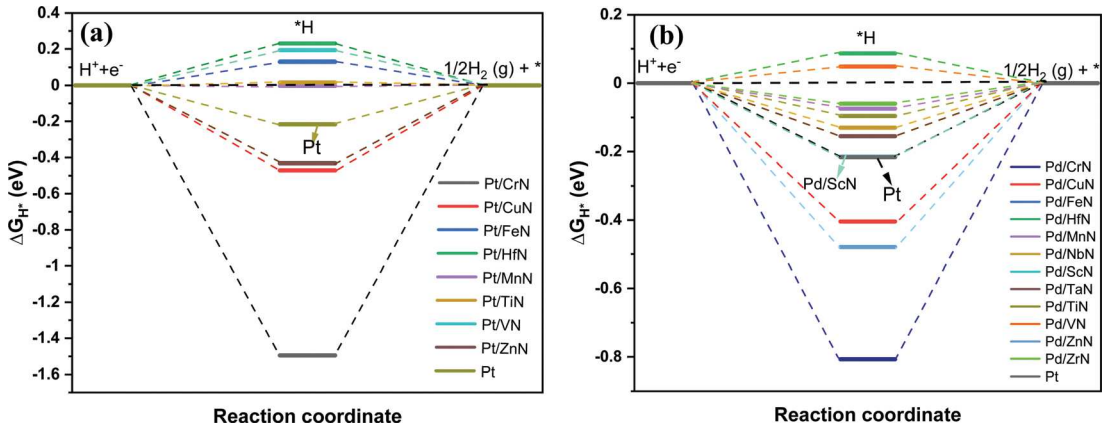

Fig. 5 (a) DFT calculated free energy diagrams of the HER at U = 0 V on (a) Pt/TMN(111) and (b) Pd/TMN(111).

catalysts. The most difficult step of the HER on Pt/MnN is the desorption of *H (*i.e.* *H → $1/2H_2(g)$ + *: the Tafel reaction), while the most difficult step of the HER on Pt/TiN is Pt/TiN is H adsorption (*i.e.* $H^+ + e^- \rightarrow$. *H: the Volmer reaction). On Pt/FeN, Pt/HfN, and Pt/VN, the ΔG_H^* values are calculated to be 0.13 eV, 0.23 eV, and 0.19 eV, respectively. These values are similar to or smaller than that on Pt $(\Delta G_H^* = 0.22\ \text{eV})$, the best performing HER catalysts.[106–108] It is noted that the most difficult step of the HER on Pt/FeN, Pt/HfN, and Pt/VN is the adsorption of H. The DFT calculations predict large ΔG_H^* values of 1.50 eV, 0.47 eV, and 0.43 eV on Pt/CrN, Pt/CuN, and Pt/ZnN, respectively. Thus, the HER is predicted to be sluggish on these candidates because of the associated large free energy barriers. The most difficult step of the HER on Pt/CuN, Pt/CrN, and Pt/ZnN is found to be the desorption of H.

Similarly, DFT calculations are performed to compute the ΔG_H^* values on Pd/TMNs. The free energy plots in Fig. 5b show that the ΔG_H^* values are comparable or even smaller on Pd/VN (0.05 eV), Pd/ZrN (0.06 eV), Pd/MnN (0.07 eV), Pd/HfN (0.09 eV), Pd/TiN (0.10 eV), Pd/NbN (0.13 eV), and Pd/TaN (0.16) than that on Pt(111). Thus, these candidates are predicted to show an excellent HER activity. Notably, the small (close to zero ΔG_H^*) values observed on Pd/ZrN (0.06 eV) and Pd/VN (0.05 eV) suggest that Pd/ZrN and Pd/VN should show superior HER performance. *H adsorption is predicted to be the rate-limiting step of the HER on Pd/HfN and Pd/VN, while the desorption of H is found to be the most difficult step of the HER on all other Pd/TMN. Our calculations show large ΔG_H^* values of 0.81 eV, 0.48 eV and 0.40 eV on Pd/CrN, Pd/ZnN, and Pd/CuN, respectively. Therefore, a sluggish HER is predicted on Pd/CrN, Pd/ZnN and Pd/CuN.

The limiting potential (U_L), defined as the lowest applied potential (U) at which all the elementary steps in free energy diagrams become downhill in energy, has been shown to correlate well with the catalytic activity of several electrochemical reactions, including the HER.[109] The DFT calculated ΔG_H^* values are used to compute the U_L on Pt/Pd–ML–TMN(111). Subsequently, a plot of U_L and HBE on Pt/Pd ML on TMN(111) is constructed (Fig. 6). The results show a volcano-like relationship between the U_L and HBE. The U_L values on Pt/MnN, Pt/TiN, Pt/FeN, Pt/VN, Pt/HfN, Pt/ZnN, Pt/CuN, and Pt/CrN are −0.003 V, −0.02 V, −0.13 V, −0.19 V, −0.23 V, −0.43 V, −0.47 V, and −1.50 V, respectively. As shown in Fig. 6, Pt/MnN and Pt/TiN lie at the top of the volcano and are predicted to be the best candidates among Pt/TMN systems. The calculated U_L values on Pt/FeN, Pt/HfN and Pt/VN are similar to that on Pt and are expected to show similar HER activity compared to Pt. The volcano plot in Fig. 6 also shows that the HBE is stronger on Pt/CrN, Pt/CuN and Pt/ZnN leading to a higher value of U_L.

A similar volcano-like relationship is observed between the U_L and HBE on Pd/TMNs. Fig. 6 shows that Pd/ZrN and Pd/VN lie closest to the top of the volcano with U_L values of −0.06 V and −0.05 V, respectively. Both Pt and Pd/ScN have a U_L value of −0.22 V. The U_L values are predicted to be −0.07 V, −0.09 V, −0.10 V, −0.13 V, and −0.16 V on Pd/MnN, Pd/HfN, Pd/TiN, Pd/NbN, and Pd/TaN, respectively. Pd/TaN, Pd/NbN, Pd/TiN, Pd/MnN, and Pd/HfN are predicted to show superior HER activity because of their smaller U_L values compared to Pt.

Fig. 6 presents a correlation between the U_L and HBE on Pt/TMN and Pd/TMN systems considered in this study. Pt/MnN and Pt/TiN lie at the top of the volcano, indicating that they efficiently catalyze the HER. The volcano-like relationship between the U_L and HBE on

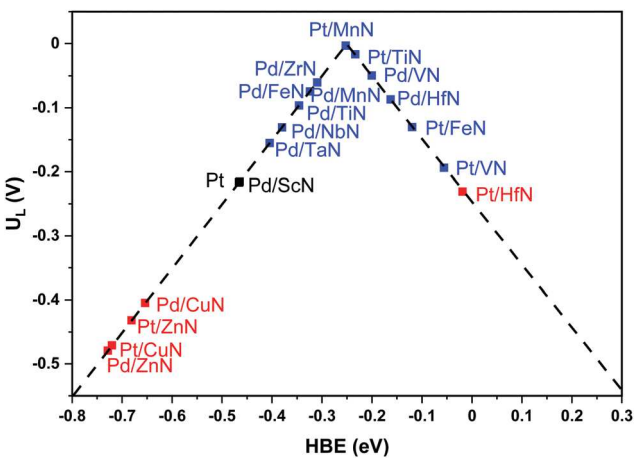

Fig. 6 Correlation between the U_L and HBE on Pt/TMNs and Pd/TMNs.

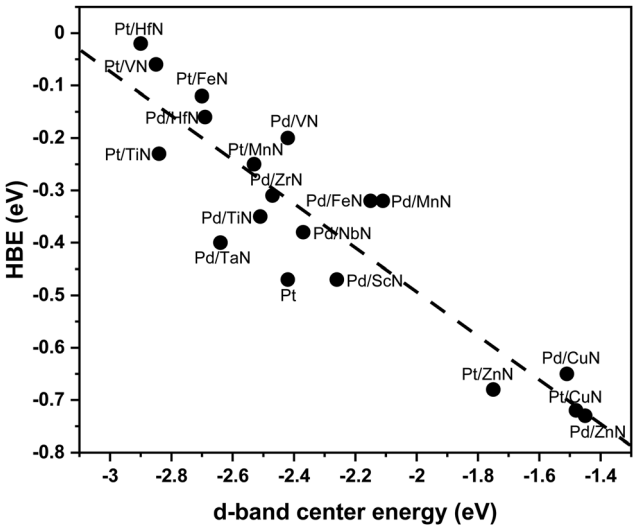

Fig. 7 Plot showing the relationship between the HBE (eV) and the d-band center (eV).

Pt/Pd-ML-TMN(111) (Fig. 6) illustrates that the candidates that have the HBE in the range of −0.47 eV to −0.06 eV should show the enhanced HER activity compared to Pt. Thus, the future HER catalyst development efforts should focus on Pt/Pd–ML–TMN(111) candidates that have the HBE in the range of −0.47 eV to −0.06 eV.

Finally, using the DFT method, we obtained the density of states (DOS) of surface Pt/Pd atoms on Pt/Pd–ML–TMN(111) and computed the d-band center as described elsewhere.[110] Our calculated d-band center shows a near-linear correlation with the HBE (Fig. 7). The weaker HBE observed on Pt/Pd–ML–TMN(111) is due to the downshifting of the d-band center compared to Pt, while the upshift in the d-band center corresponds to the observed stronger HBE. The d-band centers of the predicted best candidates are close to that of Pt, suggesting similar HER activity of these candidates compared to Pt. In contrast, the d-band centers are significantly upshifted (compared to Pt) for candidates such as Pt/CuN and Pd/ZnN, making these candidates not ideal for the enhanced HER. The observed linear correlation of the HBE (which directly correlates with the activity of the catalysts) with the d-band center suggests that the d-band center can be used as a descriptor of the HER activity on Pt/Pd–ML–TMN(111).

We performed AIMD simulations to test the thermal stability of DFT and predicted two of the best candidates (Pd/VN and Pt/TiN). The results of the AIMD simulations at 1000 K show a small fluctuation in the total energy (Fig. 8). Importantly, we observed no significant buckling of Pt and Pd overlayers (geometries in Fig. 8), indicating that Pd/VN and Pt/TiN remain stable up to 1000 K. Thus, the DFT predicted best candidates (*e.g.* Pt/TMN and Pd/TMN) are expected to be stable since the HER is typically carried out under ambient conditions with a temperature of ∼300 K.

4. Conclusions

We perform DFT calculations to investigate the HER activity of TMN@Pt/Pd core–shell catalyst structures modeled by Pt/Pd–ML–TMN(111) surfaces. The results show that several TMNs possess favorable negative formation energies as well as low surface energies for the formation of TMN(111) surfaces. Moreover, the strong binding between Pt/Pd and TMs on TMN(111) suggests that Pt/Pd–ML–TMN(111) represents a promising catalyst structure for further exploration in catalysis. We carried out additional DFT calculations to compute the hydrogen binding energy (HBE) on Pt/Pd–ML–TMN(111). The DFT calculated HBEs are then used to compute the free energy change (ΔG_H^*) along the HER pathway. Of all Pt/Pd–ML–TMN(111), our results show that Pt/MnN, Pt/TiN, Pt/FeN, Pd/TaN, Pd/NbN, Pd/HfN, Pd/MnN, Pd/ScN, Pd/VN, and Pd/ZrN have ΔG_H^* close to zero and have U_L values close to that of Pt(111). Thus, these candidates are predicted to show excellent HER activity. Furthermore, a volcano-type relationship between the DFT calculated HBE and U_L suggests that the future HER catalyst

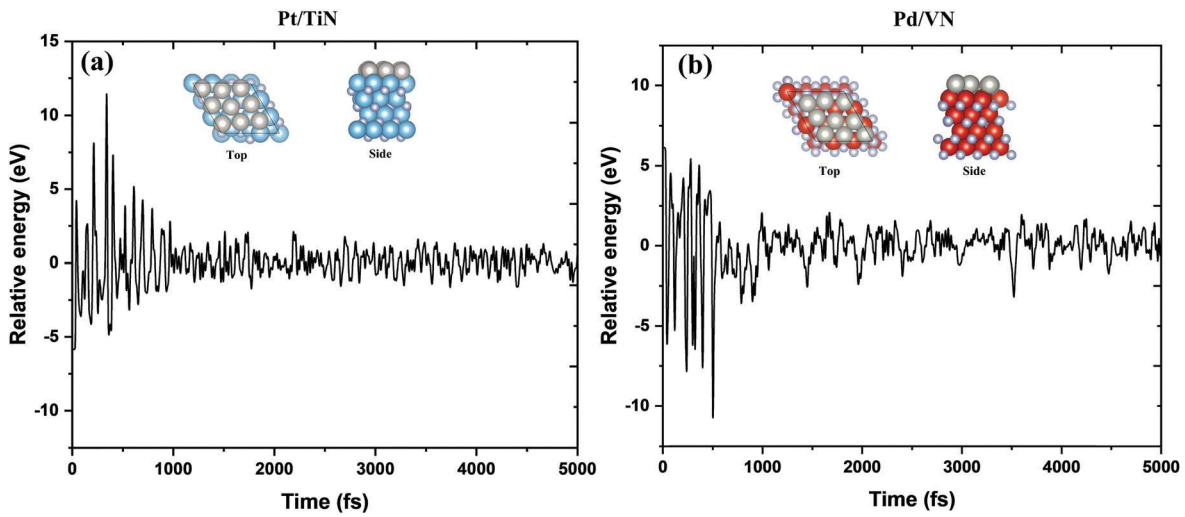

Fig. 8 Fluctuation in the total energy and snapshot of geometries (in the inset) in AIMD simulations of (a) Pt/TiNi and (b) Pd/VN at 1000 K.

development efforts should focus on Pt/Pd-ML-TMN(111) candidates that have HBE in the range of −0.47 eV to −0.06 eV.

Conflicts of interest

There are no conflicts to declare.

Acknowledgements

This work was partially supported by the National Science Foundation RIA (HRD 2055012) grant. The DFT calculations were performed using computational resources at the Extreme Science and Engineering Discovery Environment, which is supported by the National Science Foundation Grant number *ACI*-1548562. S. K. also acknowledges the faculty start-up fund from Florida A&M University.

References

1 J. Zhu, L. Hu, P. Zhao, L. Y. S. Lee and K. Wong, *Chem. Rev.*, 2020, **120**, 851–918.
2 M. Cabán-Acevedo, M. L. Stone, J. R. Schmidt, J. G. Thomas, Q. Ding, H. C. Chang, M. L. Tsai, H. He and S. Jin, *Nat. Mater.*, 2015, **14**, 1245–1251.
3 I. Staffel, D. Scamman, A. V. Abad, P. Balcombe, P. E. Dodds, P. Ekins, N. Shah and K. R. Ward, *Energy Environ.*, 2019, **12**, 463–491.
4 P. Nikolaidis and A. Poullikkas, *Renewable Sustainable Energy Rev.*, 2017, **67**, 597–611.
5 D. Li, X. Li and J. Gong, *Chem. Rev.*, 2016, **116**(19), 11529–11653.
6 A. Ersoz, *Int. J. Hydrogen Energy*, 2008, **33**, 7084–7094.
7 S. Sengodan, R. Lan, J. Humphreys, D. Du, W. Cu, H. Wang and S. Tao, *Renewable Sustainable Energy Rev.*, 2018, **82**, 761–780.
8 Q. Zhu, Y. Qu, D. Liu, K. W. Ng and H. Pan, *ACS Appl. Nano Mater.*, 2020, **3**, 6270–6296.
9 F. Barbir, *Sol. Energy*, 2005, **78**, 661–669.
10 S. A. Grigoriev, V. I. Porembsky and V. N. Fateev, *Int. J. Hydrogen Energy*, 2006, **31**, 171–175.
11 Z. Ge, B. Fu, J. Zhao, X. Li, B. Ma and Y. Chen, *J. Mater. Sci.*, 2020, **55**, 14081–14104.
12 M. Wang, Z. Wang, X. Gong and Z. Guo, *Renewable Sustainable Energy Rev.*, 2014, **29**, 573–588.
13 S. Shiva Kumar and V. Himabindu, *Mater. Sci. Energy Technol.*, 2019, **2**, 442–454.
14 Z. Li, R. Ge, J. Su and L. Chen, *Adv. Mater. Interfaces*, 2020, 7.
15 S. Ye, C. Ding and C. Li, *Adv. Inorg. Chem.*, 2019, **74**, 3–59.
16 A. Züttel, A. Borgschulte and L. Schlapbach, Hydrogen as a Future Energy Carrier, 2008.
17 S. Wang, A. Lu and C. J. Zhong, *Nano Convergence*, 2021, 8.
18 Y. Cai, A. B. Anderson, J. C. Angus and L. N. Kostadinov, *J. Electrochem. Soc.*, 2007, **154**, F36–F43.
19 S. Maheshwari, Y. Li, N. Agrawal and M. J. Janik, *Adv. Catal.*, 2018, **63**, 117–167.
20 M. T. Tang, X. Liu, Y. Ji, J. K. Norskov and K. Chan, *J. Phys. Chem. C*, 2020, **124**, 28083–28092.
21 S. Bajracharya, A. ElMekawy, S. Srikanth and D. Pant, *Microbial Electrochemical and Fuel Cells: Fundamentals and Applications*, 2016, pp. 179–213.
22 D. Tian, S. R. Denny, K. Li, H. Wang, S. Kattel and J. G. Chen, *Chem. Soc. Rev.*, 2021, **50**, 12338.
23 S. Sarkar and S. C. Peter, *Inorg. Chem. Front.*, 2018, **5**, 2060–2080.
24 H. Cheng, N. Yang, G. Liu, Y. Ge, J. Huang, Q. Yun, Y. Du, C. J. Sun, B. Chen, J. Liu and H. Zhang, *Adv. Mater.*, 2020, **32**, 1902964.
25 F. Luo, Q. Zhang, X. Yu, S. Xiao, Y. Ling, H. Hu, L. Guo, Z. Yang, L. Huang, W. Cai and H. Cheng, *Angew. Chem.*, 2018, **130**, 15078–15083.
26 R. Q. Yao, Y. T. Zhou, H. Shi, Q. H. Zhang, L. Gu, Z. Wen, X. Y. Lang and Q. Jiang, *ACS Energy Lett.*, 2019, **4**, 1379–1386.
27 J. Sun, M. Ren, L. Yu, Z. Yang, L. Xie, F. Tian, Y. Yu, Z. Ren, S. Chen and H. Zhou, *Small*, 2019, **15**, 1804272.
28 D. Y. Wang, M. Gong, H. L. Chou, C. J. Pan, H. A. Chen, Y. Wu, M. C. Lin, M. Guan, J. Yang, C. W. Chen, Y. L. Wang, B. J. Hwang, C. C. Chen and H. Dai, *J. Am. Chem. Soc.*, 2015, **137**, 1587–1592.
29 J. Wang, W. Cui, Q. Liu, Z. Xing, A. M. Asiri and X. Sun, *Adv. Mater.*, 2016, **28**, 215–230.
30 J. L. Kolar, *Environ. Qual. Manag.*, 2000, **10**, 45–54.
31 D. Bhalothia, L. Krishnia, S. S. Yang, C. Yan, W. H. Hsiung, K. W. Wang and T. Y. Chen, *Appl. Sci.*, 2020, **10**, 1–19.
32 B. H. R. Suryanto, Y. Wang, R. K. Hocking, W. Adamson and C. Zhao, *Nat. Commun.*, 2019, **10**, 5599.
33 L. Cheng, W. Huang, Q. Gong, C. Liu, Z. Liu, Y. Li and H. Dai, *Angew. Chem., Int. Ed.*, 2014, **53**, 7860–7863.
34 M. Shao, Q. Chang, J. P. Dodelet and R. Chenitz, *Chem. Rev.*, 2016, **116**, 3594–3657.
35 Q. Zhang, Z. Jiang, B. M. Tackett, S. R. Denny, B. Tian, X. Chen, B. Wang and J. G. Chen, *ACS Catal.*, 2019, **9**, 2415–2422.
36 R. Jiang, Z. Cui, W. Xu, S. Zhu, Y. Liang, Z. Li, S. Wu, C. Chang and A. Inoue, *Electrochim. Acta*, 2019, **20**, 135082.
37 S. S. Kumar and V. Himabindu, *Renewable Energy*, 2020, **146**, 2281–2290.
38 S. K. Kim, Y. Qiu, Y. J. Zhang, R. Hurt and A. Peterson, *Appl. Catal., B*, 2018, **235**, 36–44.
39 W. F. Chen, J. T. Muckerman and E. Fujita, *Chem. Commun.*, 2013, **49**, 8896–8909.
40 Y. W. Cheng, J. H. Dai, Y. M. Zhang and Y. Song, *J. Phys. Chem. C*, 2018, **122**, 28113–28122.
41 S. Meyer, A. V. Nikiforov, I. M. Petrushina, K. Köhler, E. Christensen, J. O. Jensen and N. J. Bjerrum, *Int. J. Hydrogen Energy*, 2015, **40**, 2905–2911.
42 D. Jin, L. R. Johnson, A. S. Raman, X. Ming, Y. Gao, F. Du, Y. Wei, G. Chen, A. Vojvodic, Y. Gogotsi and X. Meng, *J. Phys. Chem. C*, 2020, **124**, 10584–10592.

43 C. Yang, R. Zhao, H. Xiang, J. Wu, W. Zhong, W. Li, Q. Zhang, N. Yang and X. Li, *Adv. Energy Mater.*, 2020, **10**, 2002260.

44 Q. Zhang, Z. Jiang, B. M. Tackett, S. R. Denny, B. Tian, X. Chen, B. Wang and J. G. Chen, *ACS Catal.*, 2019, **9**, 2415–2422.

45 J. Xie and Y. Xie, *Chem. – Eur. J.*, 2016, **22**, 3588–3598.

46 B. Cao, G. M. Veith, J. C. Neuefeind, R. R. Adzic and P. G. Khalifah, *J. Am. Chem. Soc.*, 2013, **135**, 19186–19192.

47 J. Theerthagiri, S. J. Lee, A. P. Murthy, J. Madhavan and M. Y. Choi, *Curr. Opin. Solid State Mater. Sci.*, 2020, 24.

48 W. Qi, Y. Zhou, S. Liu, H. Liu, L. S. Hui, A. Turak, J. Wang and M. Yang, *Appl. Mater. Today*, 2019, 100476.

49 H. Du, R. M. Kong, X. Guo, F. Qu and J. Li, *Nanoscale*, 2018, **10**, 21617–21624.

50 S. M. El-Refaei, P. A. Russo and N. Pinna, *ACS Appl. Mater. Interfaces*, 2021, **13**, 22077–22097.

51 T. W. Wang, T. L. Wang, W. J. Chou, L. F. Wu and S. H. Lin, *Phys. Chem. Chem. Phys.*, 2021, **23**, 2305–2312.

52 X. Lv, Z. Hu, H. Zhao, Y. Liu and Z. Yuan, *Prog. Chem.*, 2018, **30**, 947–957.

53 X. Liu, X. Ge, Y. Dong, K. Fu, F. Meng, R. Si, M. Zhang and X. Xu, *Mater. Chem. Phys.*, 2020, **253**, 123334.

54 Y. Abghoui and E. Skúlason, *J. Phys. Chem. C*, 2017, **121**, 24036–24045.

55 Y. Liu, D. Tian, A. N. Biswas, Z. Xie, S. Hwang, J. H. Lee, H. Meng and J. G. Chen, *Angew. Chem., Int. Ed.*, 2020, **59**, 11345–11348.

56 S. Dutta, A. Indra, Y. Feng, H. Han and T. Song, *Appl. Catal., B*, 2019, **241**, 521–527.

57 S. A. Raheem, H. Shen, T. Thomas and M. Yang, *Phys. Chem. Chem. Phys.*, 2022, **24**, 771–777.

58 R. Zhang, Y. Zhang, X. Ren, G. Cui, A. M. Asiri, B. Zheng and X. Sun, *ACS Sustainable Chem. Eng.*, 2018, **6**, 9545–9549.

59 X. Yang, S. Kattel, J. Nash, X. Chang, J. H. Lee, Y. Yan, J. G. Chen and B. Xu, *Angew. Chem., Int. Ed.*, 2019, **58**, 13768–13772.

60 M. Yang, Z. Cui and F. D. DiSalvo, *Phys. Chem. Chem. Phys.*, 2013, **15**, 1088.

61 K. R. Yoon, K. Shin, J. Park, S. Cho, C. Kim, J. Jung, J. Y. Cheong, H. R. Byon, H. M. Lee and I. Kim, *ACS Nano*, 2018, **12**(1), 128–139.

62 T. Wu, X. Wang, A. E. Emre, J. Fan, Y. Min, Q. Xu and S. Sun, *Energy Chem.*, 2021, **55**, 48–54.

63 R. Michalsky, Y. J. Zhang and A. A. Peterson, *ACS Catal.*, 2014, **4**, 1274–1278.

64 G. Kresse and J. Furthmüller, *Comput. Mater. Sci.*, 1996, **6**, 15–50.

65 G. Kresse and J. Hafner, *Phys. Rev. B*, 1993, **48**, 13115–13118.

66 S. Equations and C. Effects, *Phys. Rev.*, 1965, **140**, 1133–1138.

67 P. E. Bloch, *Phys. Rev. B: Condens. Matter Mater. Phys.*, 1994, **50**, 17953–17979.

68 J. P. Perdew and Y. Wang, *Phys. Rev. B: Condens. Matter Mater. Phys.*, 1992, **46**, 12947–12954.

69 D. J. Chadi, *Phys. Rev. B: Condens. Matter Mater. Phys.*, 1977, **16**, 1746–1747.

70 Q. Chang, J. H. Lee, Y. Liu, Z. Xie, S. Hwang, N. S. Marinkovic, A. A. Park, S. Kattel and J. G. Chen, *JACS Au*, 2022, **2**, 214–222.

71 Z. Xie, Y. Xu, M. Xie, X. Chen, H. H. Lee, E. Stavitski, S. Kattel and J. G. Chen, *Nat. Commun.*, 2020, **11**, 1–8.

72 J. Wang, S. Kattel, C. J. Hawxhurst, J. H. Lee, B. M. Tackett, K. Chang, N. Rui, C. Liu and J. G. Chen, *Angew. Chem., Int. Ed.*, 2019, **58**(19), 6271–6275.

73 M. G. Quesne, A. Roldan, N. H. De Leeuw and C. R. A. Catlow, *Phys. Chem. Chem. Phys.*, 2018, **20**, 6905–6916.

74 J. K. Nørskov, J. Rossmeisl, A. Logadottir, L. Lindqvist, J. R. Kitchin, T. Bligaard and H. Jónsson, *J. Phys. Chem. B*, 2004, **108**, 17886–17892.

75 F. Li and Q. Tang, *ACS Appl. Nano Mater.*, 2019, **2**, 7220–7229.

76 Y. Nian, Y. Wang, A. N. Biswas, X. Chen, Y. Hou and J. G. Chen, *Chem. Eng. J.*, 2021, **426**, 130781.

77 Z. Lin, S. R. Denny and J. G. Chen, *J. Catal.*, 2021, **404**, 929–942.

78 D. Tian, S. R. Denny, K. Li, H. Wang, S. Kattel and J. G. Chen, *Chem. Soc. Rev.*, 2021, **50**, 12338–12376.

79 Q. Zhang, Z. Jiang, B. M. Tackett, S. R. Deeny, B. Tian, X. Chen, B. Wang and J. G. Chen, *ACS Catal.*, 2019, **9**(3), 2415–2422.

80 Z. Lin, R. Chen, Z. Qu and J. G. Chen, *Green Chem.*, 2018, **20**(12), 2679–2696.

81 Z. Lin, S. C. Ammal, S. R. Denny, S. A. Rkov, K. You, A. Heyden and J. G. Chen, *JACS Au*, 2022, **2**(2), 367–379.

82 Y. Liu, D. Tian, A. N. Biswas, Z. Xie, S. Hwang, J. H. Lee, H. Meng and J. G. Chen, *Angew. Chem., Int. Ed.*, 2020, **59**, 11345–11348.

83 Y. Sun, B. Yao, Q. He, F. Su and H. Z. Wang, *J. Alloys Compd.*, 2009, **479**, 599–602.

84 S. Wang, X. Yu, J. Zhang, L. Wang, K. Leinenweber, D. He and Y. Zhao, *Cryst. Growth Des.*, 2016, **16**(1), 351–358.

85 A. A. Barragan, N. V. Ilawe, L. Zhong, B. M. Wong and L. Mangolini, *J. Phys. Chem. C*, 2017, **121**(4), 2316–2322.

86 M. G. Moreno-Armenta, J. Diaz, A. Martinez-Ruiz and G. Soto, *J. Phys. Chem. Solids*, 2007, **68**, 1989–1994.

87 X. Liu, H. Lu, M. He, K. Jin, G. Yang, H. Ni and K. Zhao, *J. Alloys Compd.*, 2014, **582**, 75–78.

88 D. Ologunagba and S. Kattel, *Energies*, 2020, **13**, 2182.

89 D. V. Esposito, S. T. Hunt, Y. C. Kimmel and J. G. Chen, *J. Am. Chem. Soc.*, 2012, **134**, 3025–3033.

90 J. L. R. Yates, G. H. Spikes and G. Jones, *Phys. Chem. Chem. Phys.*, 2015, **17**, 4250–4258.

91 J. Dong, Q. Fu, Z. Jiang, B. Mei and X. Bao, *J. Am. Chem. Soc.*, 2018, **140**(42), 13808–13816.

92 H. H. Hwu and J. G. Chen, *Chem. Rev.*, 2005, **105**, 185–212.

93 B. Liu, L. Huo, R. Si, J. Liu and J. Zhang, *ACS Appl. Mater. Interfaces*, 2016, 18770–18787.

94 D. Göhl, A. Garg, P. Paciok, K. J. J. Mayrhofer, M. Heggen, Y. Shao-Horn, R. E. Dunin-Borkowski, Y. Román-Leshkov and M. Ledendecker, *Nat. Mater.*, 2020, **19**, 287–291.

95 S. T. Hunt, M. Milina, A. C. Alba-Rubio, C. H. Hendon, J. A. Dumesic and Y. Román-Leshkov, *Science*, 2016, **352**, 974–978.

96 A. Garg, M. Milina, D. Zanchet and S. T. Hunt, *Angew. Chem., Int. Ed.*, 2017, **56**, 8828–8833.

97 S. T. Hunt, M. Milina, Z. Wang and Y. Roman-Leshkov, *Energy Environ. Sci.*, 2016, **9**, 3290–3301.

98 C. Kura, Y. Kunisada, E. Tsuji, C. Zhu, H. Habazaki, S. Nagata, M. P. Muller, R. A. De Souza and Y. Aoki, *Nat. Energy*, 2017, **2**, 786–794.

99 N. A. Koratkar, *Nat. Mater.*, 2016, **15**, 1153–1154.

100 H. J. Yan, C. Tian, L. Wang, A. Wu, M. Meng, L. Zhao and H. Fu, *Angew. Chem., Int. Ed.*, 2015, **54**, 6325–6329.

101 H. Guan, W. Li, J. Han, W. Yi, H. Bai, Q. Kong and G. Xi, *Nat. Commun.*, 2021, **12**, 1376.

102 A. B. Laursen, A. S. Varela, F. Dionigi, H. Fanchiu, C. Miller, O. L. Trinhammer, J. Rossmeisl and S. Dahl, *J. Chem. Educ.*, 2012, **89**, 1595–1599.

103 K. S. Exner, *Curr. Opin. Electrochem.*, 2021, **26**, 2451–9103.

104 M. T. M. Koper and E. Bouwman, *Angew. Chem., Int. Ed.*, 2010, **49**, 3723–3725.

105 Q. Zhang, Z. Jiang, B. M. Tackett, S. R. Denny, B. Tian, X. Chen, B. Wang and J. G. Chen, *ACS Catal.*, 2019, **9**, 2415–2422.

106 N. Cheng, S. Stambula, D. Wang, M. N. Banis, J. Liu, A. Riese, B. Xiao, R. Li, T. Sham, L. Liu, G. A. Botton and X. Sun, *Nat. Commun.*, 2016, **7**, 13638.

107 C. Li and J. Baek, *ACS Omega*, 2020, **5**, 31–40.

108 B. Ruqia and S.-I. Choi, *ChemSusChem*, 2018, **11**, 2643–2653.

109 A. Kulkarni, S. Siahrostami, A. Patel and J. K. Norskov, *Chem. Rev.*, 2018, **118**, 2302–2312.

110 A. Vojvodic, J. K. Nørskov and F. Abild-Pedersen, *Top. Catal.*, 2014, **57**, 25–32.